The current issue and full text archive of this journal is available at
www.emeraldinsight.com/0961-5539.htm

Firm structure of the separated turbulent shear layer behind modified backward-facing step geometries

Masoud Darbandi, Mohammad Taeibi-Rahni and Ali Reza Naderi
Department of Aerospace Engineering, Sharif University of Technology, Tehran, Iran

Abstract

Purpose – One major challenge in turbulent flow applications is to control the recirculation zone behind the backward-facing step (BFS). One simple idea to do so is to modify the original BFS geometry, of course, without causing adverse or undesirable impacts on the original characteristics of the primary stream. The main objective of this work is to examine the solidity of the recirculation zone behind several different geometries which are slightly to moderately different from the original BFS geometry.

Design/methodology/approach – The implemented modifications cause complicated irregularities at the boundaries of the domain. The experience shows that the mesh distribution around these irregularities plays a critical role in the accuracy of the numerical solutions. To achieve the most accurate solutions with the least computational efforts, we use a robust hybrid strategy to distribute the computational grids in the domain. Additionally, a suitable numerical algorithm capable of handling hybrid grid topologies is properly extended to analyze the flow field. The current fully implicit method utilizes a physical pressure-based upwinding scheme capable of working on hybrid mesh.

Findings – The extended algorithm is very robust and obtains very accurate solutions for the complex flow fields despite utilizing very coarse grid resolutions. Additionally, different proposed geometries revealed very similar separated regions behind the step and performed minor differences in the location of the reattachment points.

Research limitations/implications – The current study is fulfilled two-dimensionally. However, the measurements in testing regular BFS problems have shown that the separated shear layer behind the step is not affected by 3D influences provided that the width of channel is sufficiently wide. A similar conclusion is anticipated here.

Practical implications – The problem occurs in the pipe and channel expansions, combustion chambers, flow over flying objects with abrupt contraction on their external surfaces, etc.

Originality/value – A novel pressure-based upwinding strategy is properly employed to solve flow on multiblocked hybrid grid topologies. This strategy takes into account the physics associated with all the transports in the flow field. To study the impact of shape improvement, several modified BFS configurations were suggested and examined. These configurations need only little additional manufacturing cost to be fabricated.

Keywords Flow, Turbulent flow, Control systems

Paper type Research paper

The authors would like to acknowledge the partial grant received from the Research Center of Sharif University of Technology.

International Journal of Numerical Methods for Heat & Fluid Flow
Vol. 16 No. 7, 2006
pp. 803-826

0961-5539
DOI 10.1108/09615530610683520

Introduction

The identification and control of shear layer reattaching regions play critical roles in many turbulent flows. They occur in many applications such as diffusers, airfoils with high angles of attack, flow over buildings, and combustion chambers. Evidently, controlling flow separation can result in considerable increase in system performance and consequently in energy saving. However, to control separation regions, a good knowledge of the flow behavior is essential. One of the most encountered reattaching turbulent shear flows is the one behind a backward-facing step (BFS). The importance of such flow has long drawn the attentions of many researchers to investigate the details of recirculation region for controlling its structure and behavior. For example, Eaton and Johnston (1981) revealed that the turbulent flow structure behind BFS depends relatively on many different factors including the boundary-layer conditions, the boundary-layer thickness before the step, the upstream or freestream turbulence intensity, the pressure gradient, and the step height. Both the past and the recent experiments indicate that the length of the separated region downstream of the step enhances with increasing the step height (Abbott and Kline, 1961; Abu-Mulaweh *et al.*, 2002). Since the valuable work of Bradshaw and Wong (1972), there have been numerous investigations in flow over BFS. Eaton and Johnston (1980) measured the length of the separated region using thermal tufts. They showed that the shear stresses were high in the separated region and that the flow was very oscillatory with low frequency therein. Also, they claimed that the required controlling parameters would not be easily predictable. Additionally, they showed that the flow oscillations damp out very rapidly near the walls (in the inner region); however, that of the outer region keeps oscillating slowly. Based on the experimental investigations performed in a fully developed turbulent flow over BFS, Kuhen (1980) indicated that the inlet flow characteristics had only minor effects on the length of the separation region. However, the channel geometry, e.g. the channel entrance height to the step height and the angle of wall channel with horizon (in the downstream region), had considerable effect on the length of the separation region. For example, Otugen (1991) investigated the effect of expansion ratio on the separated shear layer and the reattachment point. He indicates that larger step height-to-inlet channel ratios lead to higher turbulence intensities and faster growth of the unstable shear layer. Therefore, shorter normalized reattachment lengths occurred with large expansion ratios. Eaton and Johnston (1981) reviewed several measured data taken in 2D BFS flow using hot-wire, pulsed-fire and laser anemometers. The experiments were performed on different types of flow. Their collected data showed that the length of the separation region varied from 4.9 to 8.2 times the step height. In another research, Kim *et al.* (1984) showed that the separation region has many large length scales which are in the order of the height of the step. They also showed that the shear stresses drop very quickly right after the separated region and that $\overline{u'v'}$ is much higher in such flow compared with the planar mixing layer.

Beside the investigations on baseline BFS configuration, there have been some attempts from the flow control aspects. Selby *et al.* (1990) imposed a wall slip layer through the use of transpose grooves. They experimentally investigated the performance of transverse and swept grooves for controlling turbulent separated flows over a backward-facing ramp. They reported that the reattachment distance can be reduced by 20 percent over the baseline configuration. Their work showed that the

change in the width of the grooves did not considerably change the reattachment point while their heights had major effect. On the other hand, Kim and Chung (1994) experimentally investigated the effect of surface roughness on the turbulent flow field behind the step. They placed cubic roughness on the wall next to the separation region. Using different combinations of roughness spacing and roughness height, they established three different rigs and studied the length of the separation region, the averaged velocity, and its oscillation in the streamwise directions. They reported that the surface roughness on the bottom plate retarded the reattachment process by about 3.4 percent compared with that of the smooth surface. Yang and Kuo (1997) utilized numerical tools to predict the fluid flow characteristics within the recirculation zone for a BFS with uniform normal mass bleed. They used a finite-volume-based finite-difference method with power-law scheme and showed that the mass bleeds would suppress the reverse horizontal velocity, the turbulence intensity, and the Reynolds shear stress within the recirculation zone. Additionally, the reattachment point extended to downstream. Heenan and Morrison (1998) arranged a test rig and studied the BFS from an unsteady flow perspective. They showed that the global instability associated with inhomogeneous reattaching flows can be effectively removed using a suitable permeable reattachment surface. The surface extends to the point where the instantaneous velocity vector near the surface is in the downstream direction all the time.

One alternative idea for separation control behind a step is to reconfigure the overall geometry of the domain. For example, it is possible to incline the upper wall in a manner to increase the flow cross section downstream of the step (Lien and Leschziner, 1994). Additionally, Abu-Mulaweh *et al.* (2002) experimentally examined the effect of the step heights on the structure of the recirculation region. Since we do not intend to change the baseline geometry drastically, we do not consider such overall modifications in our investigation.

The numerical investigations of the modified BFS need special considerations because of the flow complexities in the vicinity of the modified boundary faces. For example, Thakur *et al.* (1996) numerically examined the turbulent flow past a BFS, followed by a rough-walled channel. To overcome the grid distribution difficulties occurred due to the large differences between the individual roughness element size and the overall flow domain, they suggested composite grids and utilized κ-ε turbulence model. Generally speaking, the grid generation for such complex solution domains can be simplified if the domain is suitably divided into several simple sub-domains. Then, each sub-domain can be filled in with only one type of element and in a manner which automatically fits the boundaries of that sub-domain (Davidson, 1996). In a recent research, the current workers were assured that the hybrid grid usage in laminar flow cases could remarkably enhance the efficiency of the basic numerical procedure without jeopardizing its benefits (Darbandi *et al.*, 2003b; Darbandi and Naderi, 2006). In this work, the original hybrid method is suitably extended to turbulent reattaching flow applications where hybrid grid utilization is almost unavoidable. Since the current method is a finite-volume-based finite-element method, it is possible to use both quadrilateral and triangular elements. To change the geometry of the step, we have considered several different choices including the insertion of a mini channel between the upstream and downstream of the step. The use of hybrid grid not only eases the mesh generation procedure but also assures several side

benefits. For example, the use of quadrilateral grid close to the wall assures the non-oscillatory pressure field behavior in the domain. The main purpose of this work is to establish a study on the firmness of the reattachment point behind the step despite imposing different geometry modifications around the baseline configuration.

Domain discretization

In the finite-volume-based finite-element method, it is customary to utilize the finite-element shape functions which are ingredient of the finite-element method. This feature enables the finite-volume method to gain the geometrical flexibility of the finite-element method. Therefore, from domain discretization point of view, we stick to the approach taken routinely in the finite-element method. There are generally two choices of triangular and quadrilateral elements in the finite-element method. The finite-element methods normally utilize only one type of element shape to discretize the solution domain. Each type has its own advantages and disadvantages. Generally speaking, triangles are more flexible than quadrilaterals because they can be used in complex geometries simply. However, the triangular-based mesh essentially suffers from grid orientation plague (Baliga and Patankar, 1983; Darbandi *et al.* 2003a). On the contrary, the quadrilateral-based topologies are easier to be generated. Also, non-oscillatory pressure and velocity fields are less possible to occur in quadrilateral topologies. We can benefit the advantages of both element types if they are suitably distributed in the sub-domains of a complex solution domain which is properly broken into multiblocks. For example, Figure 1(a) shows the region close to the step of an inclined BFS. In this figure, we have used non-uniform hybrid grid within a structured context to distribute our grids desirably. As is observed, the triangles can be readily fitted in the triangular block. Alternatively, the advantages of both element shapes can be also utilized in flow fields with different flow characteristics in different parts of the domain. For example, the grid distributions beside the solid walls play critical role in achieving accurate turbulent flow solution in the domain. A non-uniform structured grid distribution using quadrilaterals nearby the solid walls has been highly recommended (Figure 1(b)) (Kim and Choi, 2000; Darbandi and Naderi, 2006). The use of an unstructured grid in the rest of domain helps to reduce the computational effort for a specified accuracy.

Figure 2 shows a small part of a solution domain consisted of four quadrilateral and three triangular elements. It might be a part of grid shown in Figure 1. The solid lines denote the elements while the dashed lines are their medians. The medians divide each triangular element into three and each quadrilateral element into four sub-control volumes (SCVs). The proper assemblage of the SCV around a chosen node results in a control volume, see the shaded area in Figure 2. The node at the center of the element is a good representative of the entire constructed control volume. In the next section, it will be seen that it is required to calculate the convection and diffusion fluxes at midpoints of the dashed lines, i.e. at the cell faces. The fluxes are calculated at the integration points which are identified by ip. They are indicated as ip1 and ip2 for SCV1 in Figure 2.

Governing equations and computational modelling

The steady 2D transport equation for a general property φ can be written as:

$$\frac{\partial}{\partial x}(\rho u\varphi) + \frac{\partial}{\partial y}(\rho v\varphi) = \frac{\partial}{\partial x}\left[\Gamma_\varphi \frac{\partial \varphi}{\partial x}\right] + \frac{\partial}{\partial y}\left[\Gamma_\varphi \frac{\partial \varphi}{\partial y}\right] + S_\varphi \tag{1}$$

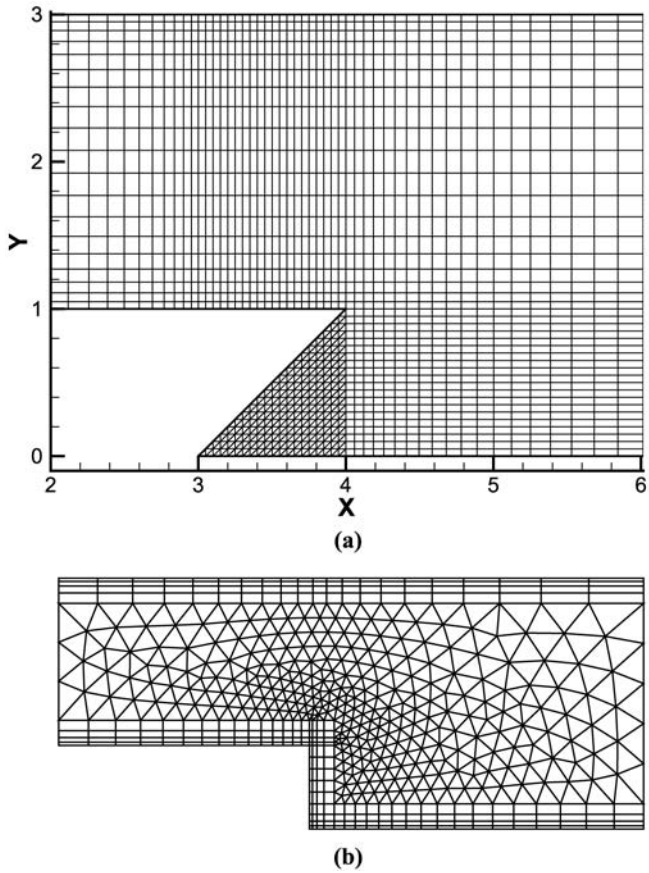

Figure 1.
Two types of hybrid mesh utilizations in: (a) irregular; and (b) baseline BFS domains

The components of the velocity vector are u and v. Table I provides the details of general property φ, diffusivity coefficient Γ_φ, and source term S_φ for the mass, momentums, turbulent kinetic energy (TKE), and the dissipation rate of TKE equations. The two G and μ_e parameters in Table I represent the production term and the turbulent viscosity coefficient, respectively. They are given by:

$$\mu_e = \mu_l + \mu_t = \mu_l + \rho C_\mu \frac{k^2}{\varepsilon} \tag{2}$$

$$G = \mu_t \left\{ 2\left[\left(\frac{\partial u}{\partial x}\right)^2 + \left(\frac{\partial v}{\partial y}\right)^2 \right] + \left(\frac{\partial u}{\partial y} + \frac{\partial v}{\partial x}\right)^2 \right\} \tag{3}$$

The density, dynamic viscosity, and eddy viscosity are represented by ρ, μ_l, and μ_t, respectively. As is indicated in Table I, we use standard κ-ε model to simulate turbulent flow. The correlating constants in this model are $C_1 = 1.44$, $C_2 = 1.92$, $C_\mu = 0.09$, $\sigma_\kappa = 1.0$, and $\sigma_\varepsilon = 1.3$. Because of the inaccuracy of the κ-ε turbulence model close to the solid walls of the BFS, it is required to use suitable supplementary

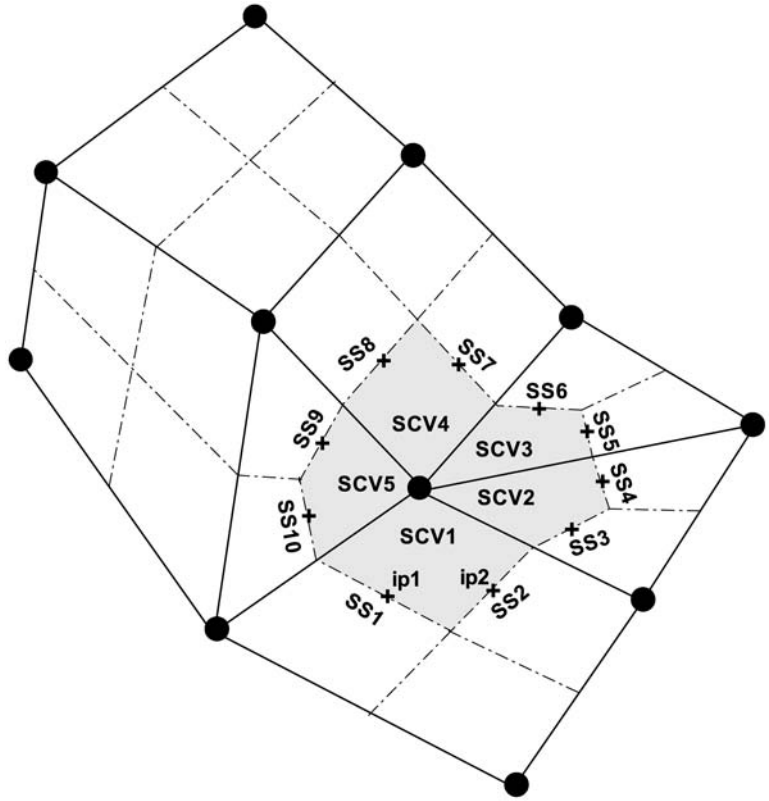

Figure 2.
A control volume constructed from the assemblage of five SCVs

Equation	φ	Γ_φ	S_φ
Mass	1	0	0
x-momentum	u	μ_e	$-\left(\frac{\partial p}{\partial x}\right)+\frac{\partial}{\partial x}\left(\mu_e\frac{\partial u}{\partial x}\right)+\frac{\partial}{\partial y}\left(\mu_e\frac{\partial v}{\partial x}\right)$
y-momentum	v	μ_e	$-\left(\frac{\partial p}{\partial y}\right)+\frac{\partial}{\partial x}\left(\mu_e\frac{\partial u}{\partial y}\right)+\frac{\partial}{\partial y}\left(\mu_e\frac{\partial v}{\partial y}\right)$
Turbulence kinetic energy	κ	μ_e/σ_κ	$G-\rho\varepsilon$
Dissipation rate of κ	ε	μ_e/σ_ε	$\varepsilon(C_1G-C_2\rho\varepsilon)/\kappa$

Table I.
The definitions of φ, Γ_φ, and S_φ in equation (1)

wall function there. We employ the standard two-layer form of the law of the wall (Thangam and Speziale, 1992):

$$\bar{u}^+ = \frac{1}{K}\ln y^+ + 5, \quad \frac{\kappa}{u_\tau^2} = C_\mu^{-1/2}, \quad \varepsilon = C_\mu^{3/4}\frac{\kappa^{3/2}}{Ky}$$

at the first grid point y away from the wall if $y^+ \equiv yu_\tau/v \geq 11.6$ given that $\bar{u}^+ \equiv \bar{u}/u_\tau$ (u_τ is the friction velocity and $K = 0.41$ is von Karman constant); if $y^+ < 11.6$, then $\bar{u}$, κ, and ε are interpolated to their wall values based on viscous sublayer constraints (Amano, 1984).

The transport equation is integrated over an arbitrary control volume consisted of SCVs taken from either quadrilateral or triangular elements. The chosen control volume in Figure 2 consists of five SCVs numbered from SCV1 to SCV5. Using the divergence theorem, the volume integration on a control volume can be reduced to an assemblage of line integrals over the boundaries of that chosen volume. The boundary of the chosen control volume in Figure 2 consists of ten sub-surfaces, i.e. SS1-SS10. For the sake of brevity, we only present the formulation for an individual SCV, i.e. SCV1, which only has two subsurfaces, i.e. SS1 and SS2. Considering the above explanations, the integration of the convection terms in equation (1) over SCV1 yields:

$$\int_{\mathrm{SCV1}}\left[\frac{\partial}{\partial x}(\rho u\varphi)+\frac{\partial}{\partial y}(\rho v\varphi)\right]\mathrm{d}x\,\mathrm{d}y \cong [(\rho\bar{u}\varphi)\Delta S_x+(\rho\bar{v}\varphi)\Delta S_y]_{\mathrm{SS1}} + [(\rho\bar{u}\varphi)\Delta S_x+(\rho\bar{v}\varphi)\Delta S_y]_{\mathrm{SS2}} \tag{4}$$

where $\vec{\mathrm{d}S}=(\Delta S_x)\hat{i}+(\Delta S_y)\hat{j}$ is an outward normal vector to the face of each subsurface. Here, the over bar indicates that the variable is approximated from its known magnitude obtained at the preceding iteration. Later, we will show that the magnitude of φ in equation (4) is approximated at SS1 and SS2 using a pressure-weighted physical-influence scheme developed by Darbandi and Schneider (1998) for the laminar flow applications. In this scheme, the role of pressure is implicitly forced in approximating the magnitude of φ at the cell faces.

The integration of the diffusion part in equation (1) over SCV1 yields:

$$\int_{\mathrm{SCV1}}\left[\frac{\partial}{\partial x}\left(\Gamma_\varphi\frac{\partial\varphi}{\partial x}\right)+\frac{\partial}{\partial y}\left(\Gamma_\varphi\frac{\partial\varphi}{\partial y}\right)\right]\mathrm{d}x\,\mathrm{d}y \cong \left[\left(\Gamma_\varphi\frac{\partial\varphi}{\partial x}\right)\Delta S_x+\left(\Gamma_\varphi\frac{\partial\varphi}{\partial y}\right)\Delta S_y\right]_{\mathrm{SS1}} + \left[\left(\Gamma_\varphi\frac{\partial\varphi}{\partial x}\right)\Delta S_x+\left(\Gamma_\varphi\frac{\partial\varphi}{\partial y}\right)\Delta S_y\right]_{\mathrm{SS2}} \tag{5}$$

The gradients of φ appeared in the right-hand-side of equation (5) are then approximated using the gradients of finite-element shape functions.

The source terms in the momentum equations are a combination of different gradients of φ and pressure p parameters. They are treated very similar to the diffusion terms in equation (5). However, the source terms in κ and ε equations need special attention. The integrals of these source terms are approximated at the cell centers. Using a mass-lumped approach, the integrations yield:

$$S_\kappa=\int_{\mathrm{SCV1}}(G-\rho\varepsilon)\mathrm{d}x\,\mathrm{d}y\cong(G-\rho\varepsilon)A_{\mathrm{SCV1}} \tag{6}$$

$$S_\varepsilon=\int_{\mathrm{SCV1}}\frac{\varepsilon}{\kappa}(C_1G-C_2\rho\varepsilon)\mathrm{d}x\,\mathrm{d}y\cong\frac{\varepsilon}{\kappa}(C_1G-C_2\rho\varepsilon)A_{\mathrm{SCV1}} \tag{7}$$

where $A=\sum_i A_{\mathrm{SCV}i}$ is the total area in the chosen control volume, see the shaded area in Figure 2. The most difficult part in equations (6) and (7) is the calculation of G. Considering a mass-lumped approach, this term is calculated at the cell center using the gradients of the finite-element shape functions. Using finite-element shape functions N, the κ and ε at the cell faces are similarly calculated using:

$$\kappa = \sum_{j=1}^{3\text{or}4} (N_j)_{\text{ip1,ip2}} \kappa_j$$
$$\varepsilon = \sum_{j=1}^{3\text{or}4} (N_j)_{\text{ip1,ip2}} \varepsilon_j \tag{8}$$

where j counts the number of nodes in each element. It can be three and four for the triangular and quadrilateral element choices, respectively. The ip1 and ip2 indicate the midpoints of SS1 and SS2 cell faces. They are shown using cross symbol in Figure 2. It should be notified that the two source terms in κ and ε equations are explicitly calculated from the known magnitudes obtained during the last iteration.

One critical stage in finite-volume method is to interpolate the cell face magnitudes, i.e. the magnitudes at the integration points, from the magnitudes of neighboring grid points. Inspecting equation (4), we need calculating velocity components at SS1 and SS2. However, we should be very careful in interpolating the velocities and not ignore the important role of convection-diffusion concept. To respect the correct physics of the convection, Darbandi and Schneider (1998) employed a pressure-weighted upwind-biased scheme (known as a physical influence scheme) on quadrilateral grids. To model the correct physics of the convection, the convection term in equation (4) is upwinded. Considering an arbitrary ith cell face in Figure 2, one inclusive expression can be suggested as:

$$\phi_i = \phi_k + \left(\frac{\partial \phi}{\partial s}\right)_i \Delta S_{ki} \tag{9}$$

This expression has been written in the streamwise direction at mid-point of the ith cell face. The length ΔS_{ki} is a geometry sensitive parameter. The subscript k denotes the upstream of the ith cell-face. We have to determine the gradient of ϕ along the streamline in equation (9). We try to approximate this gradient using the original governing PDE's. In this regard, one meaningful approximation can be suggested by writing the revised momentum equations in the streamwise direction, i.e.:

$$\rho V_{\text{tot}} \frac{\partial \phi}{\partial s} = \nabla \cdot (\mu \nabla \phi) + S_\phi \tag{10}$$

where $V_{\text{tot}} = \sqrt{\bar{u}^2 + \bar{v}^2}$ is the total velocity at the cell mid-point and the source term S_ϕ represents either $\partial p/\partial x$ in treating x-momentum equation or $\partial p/\partial y$ in treating y-momentum equation. The substitution of equation (10) in equation (9) results in:

$$\phi_i = \phi_k + \left[\frac{1}{\rho V_{\text{tot}}} (\nabla \cdot (\mu \nabla \phi) + S_\phi)\right]_i \Delta S_{ki} \tag{11}$$

As is observed, the influence of pressure has been considered in calculating the correction part of equation (9) now. Using the finite-element ingredient, this statement can be discretized to:

$$\phi_i = \sum_{j=1}^{3\text{or}4} (N_j)_k \Phi_j + \frac{1}{\rho (V_{\text{tot}})_i} \left(\frac{\sum_{j=1}^{3\text{or}4} (N_j)_i \Phi_j - \phi_i}{L_i^2} - \sum_{j=1}^{3\text{or}4} \left.\frac{\partial N_j}{\partial z}\right|_i P_j \right) \Delta S_{ki} \tag{12}$$

where L_i is an appropriate diffusion length scale. This length can be estimated within an element by discretizing the diffusion terms using suitable central difference schemes in x- and y-directions (Darbandi and Schneider, 1998).

Equation (12) shows that ϕ_i appears in both sides of equation. A suitable rearrangement of the new equation in terms of our major dependent variables, i.e. Φ_j and P_j, finally yields:

$$\phi_i = \sum_{j=1}^{3 \text{ or } 4} \alpha_{ij} \Phi_j + \sum_{j=1}^{3 \text{ or } 4} \beta_{ij} P_j + \gamma_i \tag{13}$$

where the subscript i denotes the number of cell faces within an element (Figure 2). The parameters α, β, and γ represent two 3×3 (or 4×4) matrices, and one 3×1 (or 4×1) array of coefficients, respectively. These coefficients measure the weights of pressure and velocity fields on the cell-face magnitude. Equation (13) indicates that $\phi(\equiv u, v)$ at cell-face can be approximated by the proper assemblage of $\Phi(\equiv U, V)$ and P magnitudes at the cell centers of an element which surrounds the ith cell face magnitude. In fact, this approximation is known as the pressure-weighted upwinding scheme.

Following the description provided in the Domain discretization section, the current grid is a collocated one. As is known, the pressure-based algorithm suffers from the pressure checkerboard problem if they are normally treated on collocated grids. One remedy is to use the dual-velocity definitions at the cell faces. In this regard, we use the idea of Darbandi and Bostandoost (2005) which provides a wide range of velocity definitions to be employed at the cell faces of collocated grid arrangements. Using this idea, one set of the velocity components is plugged in the continuity equation and another set of the velocities in the rest of equations. These substitutions suppress the spurious pressure oscillations in the domain.

At the end of the discretization procedure, the discretized equations are solved in a bi-implicit manner (Darbandi *et al.*, 2004). At the first step, the continuity and momentum equations are implicitly solved to calculate the pressure and velocities, respectively. At the second stage, the TKE and its dissipation rate equations are implicitly solved to calculate κ and ε (Darbandi *et al.*, 2005). Considering the nonlinear nature of the discretized equations, it is required to iterate the extended bi-implicit procedure until the magnitudes of the specified residuals become sufficiently low.

The basic configuration and its modifications

As was elaborated in the Introduction section, the BFS flow problem occurs in many practical engineering applications. The importance of this flow has led to several important benchmark test cases which can be used to improve the advances in turbulence modeling and to validate the newly developed numerical algorithms. Owing to its complexities, there are numerous available publications which study this test case either experimentally or numerically. Figure 3 shows the baseline geometry of a BFS. Let us call it BS case. The longitudinal length is not exactly scaled in this figure. Following the experimental data reported by Kim *et al.* (1984), the step height, the inlet height, and the channel length are $h = 1$, $2h$, and $28h$, respectively. However, to achieve our goal, we need considering various entrance lengths $4h \leq b \leq 5h$ in our

study. Their limiting cases are identified as BS1 (with $b = 4h$) and BS2 (with $b = 5h$). In this study, all dimensions are given with respect to the step height. In another words, all the lengths are nondimensionalized using the step height h. In our study, the Reynolds number of the flow (based on the step height and the average inlet velocity) is 69,610. At the solid walls, no slip boundary condition is employed. However, κ and ε are found using standard wall functions. At the inlet, the profiles of velocity, κ, and ε are specified. The details can be found in Kim *et al.* (1984). At the outlet, the pressure is specified.

As is known, the turbulent flow behind BFS involves several important phenomena such as separation and reattachment regions and mixing-layer evolution. From the mixing point of view, there have been numerous attempts to enhance the fluid mixing behind the step. Following the past works mentioned earlier in the Introduction section, we are also willing to study and control the separated shear layer behind the step by trimming the step's geometry. In this regard, the geometry around the step corner is suitably modified. We have imposed several restrictions in our modification, e.g. the new geometry should be cost effective from manufacturing perspective, the inlet and outlet flow characteristics should not be altered, and supplementary suction (or blowing) is not permitted.

In this work, four different extended geometries are investigated. They are called A, B, C, and D (Figure 4). In type A, the sharp edge of the corner is suitably trimmed. The results of three different cases of A, i.e. A1, A2, and A3, are presented here. In this type, $b = 4.9$, 4.5, and 4.0 and $a = 0.1$, 0.5, and 1.0 for A1, A2, and A3 cases, respectively. In type B, we study the effect of a rectangular groove located upstream of the step. We consider three different B1, B2, and B3 groove geometries here. In these cases, the inlet length is $b = 5.0$ while the distances between the inlet and the grooves are 4.0, 4.3, and 4.3 and the groove heights are 0.5, 0.5 and 0.2 for B1, B2, and B3 choices, respectively. In case B3, the groove height is low and located nearby the separation point. In type C, the baseline configuration is modified by inserting a secondary channel between the upstream and downstream of the step. Type C involves two cases of C1 and C2. As is explained later, the former one acts like blowing while the latter behaves like a suction. A proper combination of A3 and C2 configurations results in a new type of geometry called type D. In cases C1, C2, D1, and D2, the magnitudes of b, $L1$, $L2$, and $h2$ are 4.0, 0.1, 1.0, and 0.1, respectively. The height $h1$ is zero in C1 and D1 cases while it is 0.1 in C2 and D2 cases.

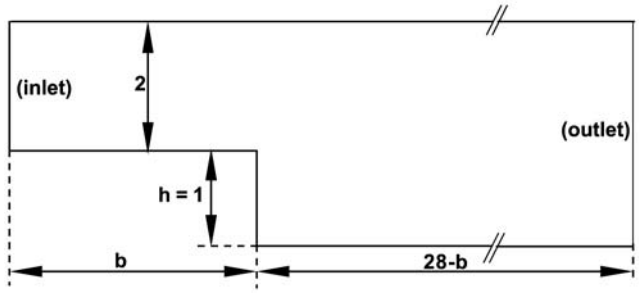

Figure 3.
A schematic of the baseline BFS geometry identified as the BS case

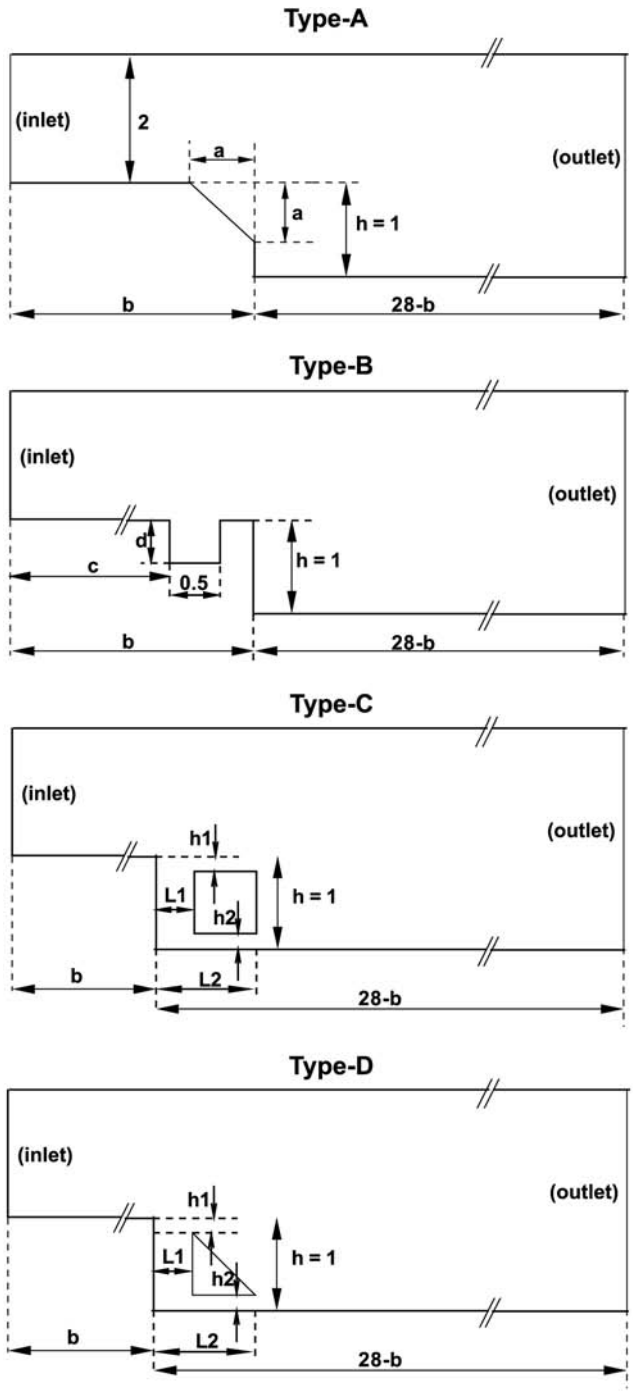

Figure 4.
Schematics of different modified BFS geometries

Results and discussion

Before presenting the results for our different BFS configurations, it is required to validate the results of our extended algorithm. In this regard, we choose two test cases which have been numerically solved by the past workers using the two-equation κ-ε turbulence model. The first test case is taken from Westphal *et al.* (1984). This test case has been numerically solved by Ilinca and Pelletier (1999) using two different two-equation turbulence models including the κ-ε and κ-ω ones. Following the description given in the preceding section, the second test case is our baseline BFS configuration which has been taken from Kim *et al.* (1984). This test case has been numerically solved by Sohn (1988).

The geometry and boundary conditions of the first test case is taken from Ilinca and Pelletier (1999). Using a step height of h, the height of channel, the length of channel, the length of channel downstream of the step are $2.5h$, $24h$, and $20h$, respectively. The Reynolds number based on the inlet mean velocity is $Re = (Uh)/\nu = 42,000$. The inlet turbulence intensity is set to $\kappa/U^2 = 0.02$. The problem is tested using three different grid resolutions from coarse Grid 1 to fine Grid 3. The details of three grid resolutions are given in Table II. In this table, NI1 and NI2 indicate the number of nodes in the longitudinal directions at upstream and downstream of the step, respectively. Similarly, NJ1 and NJ2 indicate the number of nodes in the transversal directions at upstream and downstream of the step, respectively. The table also shows that the number of nodes is almost doubled from Grid 1 to Grid 2 and from Grid 2 to Grid 3. The number of nodes in Grid 3 is almost one-half of that utilized by Ilinca and Pelletier (1999) in their fine grid.

Figure 5 shows the streamlines and TKE contours in the domain using fine Grid 3. Qualitatively, they are similar to those of the references. Quantitatively, the length of the recirculation region is about $6.5h$. Westphal *et al.* (1984) experimentally measure this length and report it as $(7.33 \pm 1.0)h$. Ilinca and Pelletier (1999) indicate that their predictions using the κ-ε model are closer than that of the κ-ω model to the experimental data on their adapted meshes. Their best results predict a recirculation length of $6.47h$.

Following the measurements of Westphal *et al.* (1984) and the numerical solution of Ilinca and Pelletier (1999), we also present the velocity and the TKE profiles at

Table II.
The grid resolution in the three utilized meshes

	NI1	NI2	NJ1	NJ2	Total nodes
Grid 1	17	81	27	45	4,023
Grid 2	25	101	37	65	7,389
Grid 3	45	129	47	85	12,951

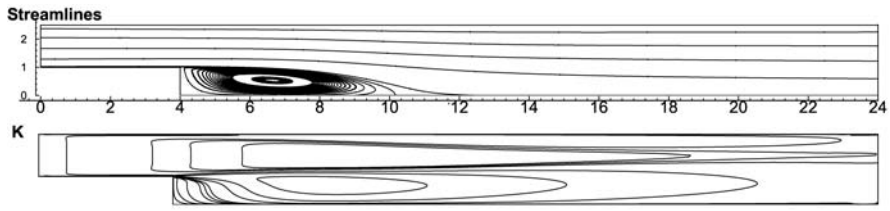

Figure 5.
The streamlines and TKE contours in the domain of the first test case, $Re = 42,000$

two longitudinal locations downstream of the step $x/h = 4.0$ and 12.0. The results are observed in Figure 6. To illustrate the mesh independence of the solutions, we have presented the results for the three chosen grids. As is observed, the numerical solutions approach their final distributions as mesh is gradually refined. In another words, the figure indicates that Grid 3 is fine enough to guarantee mesh independent solution. The figure also indicates that the current results are in good agreement with the numerical solution and the experimental data. It should be notified that our results are very close to those of Ilinca and Pelletier (1999) who similarly employ κ-ε turbulence model in their simulation.

As was described earlier, the second test case is the experiment of Kim *et al.* (1984). Although the solution domain in this test case is a bit different from the first test case, we solved the problem using different grid resolutions given in Table II. The qualitative distributions of isobars, iso-TKEs, and streamlines have been in excellent agreement with those of past workers. The details of the reattachment length

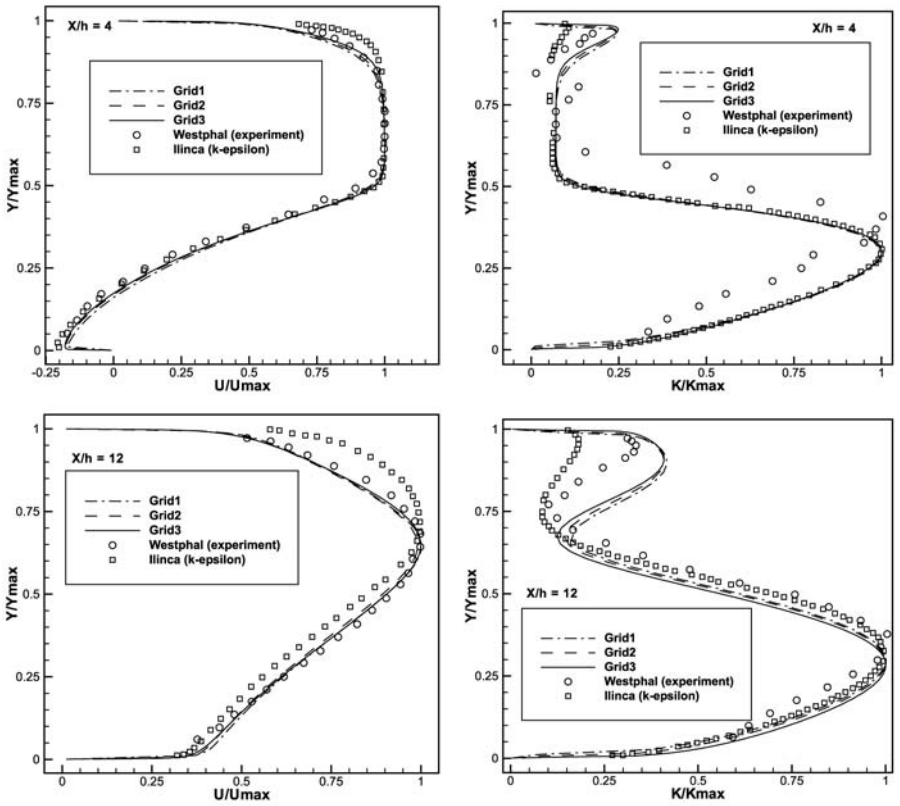

Note: The longitudinal velocity and turbulent kinetic energy profiles at two different longitudinal locations and comparing them with the available experimental data and another numerical solution, test case 1, Re = 42,000

Figure 6.

are given shortly. However, the velocity and TKE's profiles are shown in Figure 7 and compared with those of numerical solution and experimental data. Similar to the conclusions obtained in Figure 6, the current solutions are in suitable agreement with those of two-equation κ-ε model presented by Sohn (1988). Figure 7 also provides the results of mesh refinement study. As is seen, Grid 3 is fine enough to result in mesh independent solution at all longitudinal locations.

The next stage is to validate the accuracy of our hybrid grid solutions. To achieve this, we examined both pure quadrilateral and hybrid grid topologies with identical mesh node numbers. As is shown in Figure 1, we have used the quadrilateral elements nearby the solid walls in our hybrid grid choice. The rest of the domain is covered with triangles. Following our preceding discussion, using this type of hybrid grid topology considerably improves the solution nearby the solid boundaries. Also, the difficulties of the mesh orientation are automatically resolved (Darbandi *et al.* 2003a). Figure 8 shows the mean velocity profiles at three different stations downstream of the step. The results are compared with those of Kim *et al.* (1984) and Sohn (1988). As is seen, the results of our hybrid and quadrilateral grid topologies are nearly the same. This conclusion indicates that the accuracy of our original formulation is not deteriorated in extending to hybrid grid applications. As was explained earlier, Darbandi *et al.* (2003b) developed the original formulation to solve the laminar flow fields using hybrid grids. They showed that the achieved accuracy is excellent in treating laminar flow cases. Similarly, the achieved accuracy in solving turbulent flow is also comparable with that of the laminar flow case. Comparing the results of quadrilateral and hybrid grid topologies in Figure 8, it reveals that there is no disturbance at or around the boundaries between the two adjacent mesh blocks.

As was mentioned in the Introduction section, Kuhen (1980) showed that the distance between the separation point and the inlet flow b had little effect on the length of the separation region. Although our channel geometry is different than Kuhen's, we similarly tested the effect of changing b from $4h$ to $5h$ in all chosen configurations. Figure 9 shows the streamlines in the baseline geometry using two different b lengths. The results of both cases indicate that the length of the separation region is almost the same and it is about $6.1h$. The figure also compares the mean velocity profiles for cases BS1 and BS2 at three different locations ($x/h = 1.33$, 5.33, and 8.0) downstream of the step. These locations are measured from the step in each case. This figure also shows that the distance b slightly affects the mean velocity profiles in the separated shear layer behind the step.

Figure 10 shows the streamlines obtained after solving the A cases. A careful calculation shows that the length of the separation region is about 5.7 times the step height in all these cases. However, the mixing region decreases with respect to BS1 case going from case A1 to case A3. This figure also presents the mean velocity profiles of A cases at three locations downstream of the step. The distances are measured from the step's top corner which is fixed in all the three cases. In this figure, the mean velocity profiles of A cases are compared with the mean magnitudes of BS1 case. As is seen, the profiles of cases A are nearly identical. The differences between the results at the first station ($x/h = 1.33$) are hardly distinct, while the differences are considerable at the second and third stations.

Figure 11 shows the streamlines using B cases. A careful examination indicates that the length of the separation region is the same in these three cases and it is about 5.7 times the step height. However, the mixing region decreases with respect to BS1 case going from case B1 to case B3. The figure also illustrates the mean velocity profiles at three

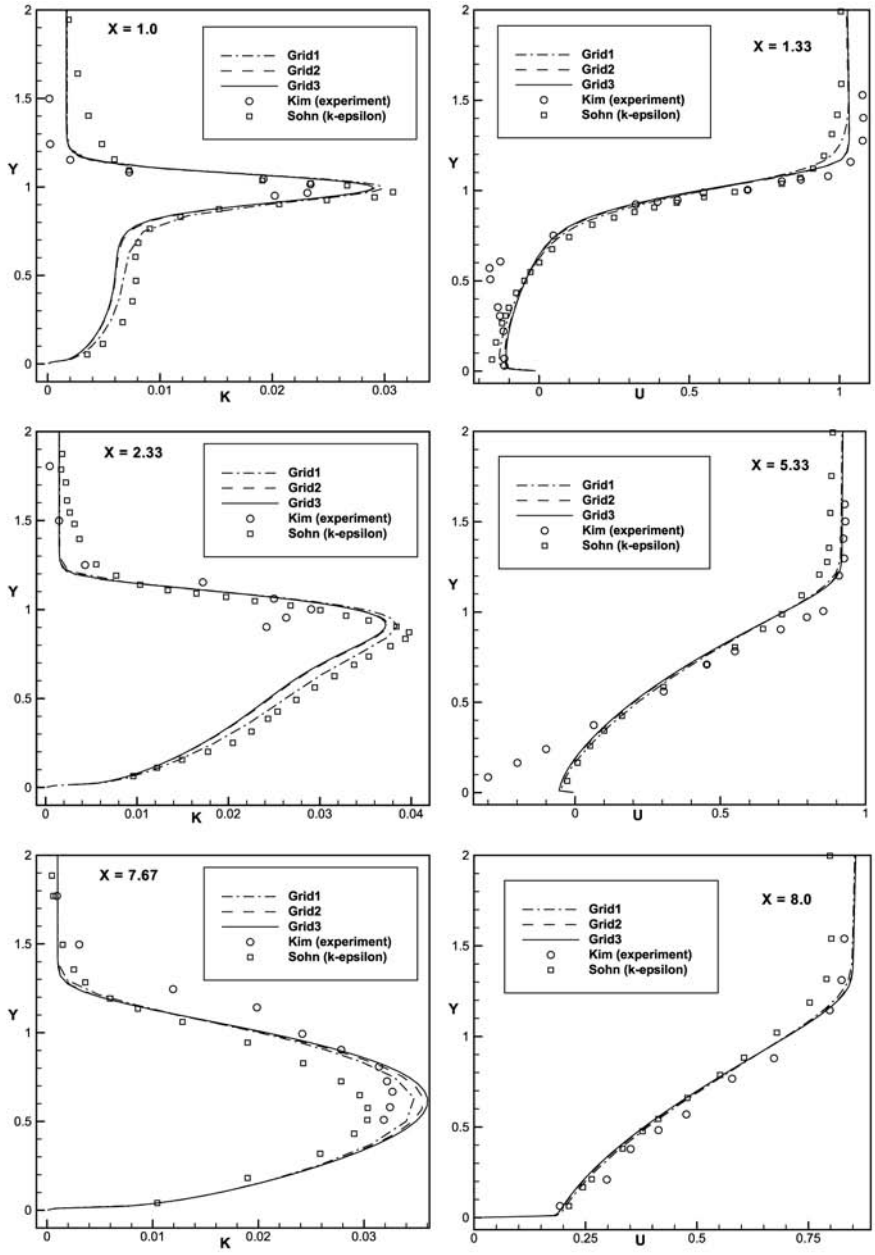

Note: The longitudinal velocity and turbulent kinetic energy profiles at different longitudinal locations and comparing them with the other available experimental data and numerical solution, test case 2, Re = 69,610

Figure 7.

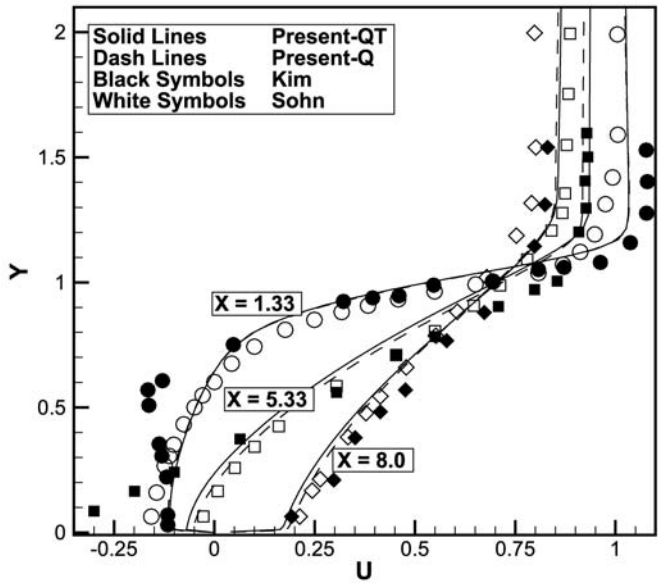

Figure 8.
Comparing the results of quadrilateral and hybrid grid topologies with those of Kim *et al.* (1984) and Sohn (1988) at three stations downstream of the step

different stations using B1, B2, and B3 cases. The current profiles are also compared with case BS2 in this figure. The location of these sections are measured from $x/h = 5$. The figure shows that the profiles of all B cases are exactly the same at all three stations. However, their deviations from the standard BS2 case are considerable.

Figure 12 shows the streamlines resulted from testing C1 and C2 cases. These two tests showed that the C1 case would perform a blowing effect and the C2 case a suction effect. The suction and blowing behaviors return to the pressure differences between the two terminals of the inserted channel. As is observed, the length of the separation region in case C2 is obviously shorter than the BS1 case and case C1 performs little changes relative to BS1 case. The length of the separation region in case C1 is 5.7 times the step height while it is 5.3 in case C2. This figure also demonstrates the mean velocity profiles of C cases and compares them with BS1 case at three chosen sections downstream of the step. The location of the sections are determined from $x/h = 5$. In all sections, the mean velocity profiles of cases C can be clearly distinct from case BS2, although cases C1 and C2 do not behave similarly. The difference between case C2 and BS2 is more than that between cases C1 and BS2.

Figure 13 shows the streamlines of case D2 which is a combination of A3 and C2 configurations. The test showed that this case would perform a suction effect. The length of the separation region is about 5.7 times the step height. The figure also shows the mean velocity profiles of cases D2 and compares them with that of case BS1 at the three utilized stations downstream of the separation points. The distances are measured from the top corner where the separation begins, i.e. $x/h = 4$. The mean velocity profiles are quite different from those of BS1 case shown at $x/h = 5.33$ and 8.0.

Back to Figure 10, we have identified two lengths, i.e. L_S and L_T, for case A2. They indicate the distances from the reattachment point to either top or bottom corners of the step. We indicate R as the length of the separation region in cases BS1 or BS2.

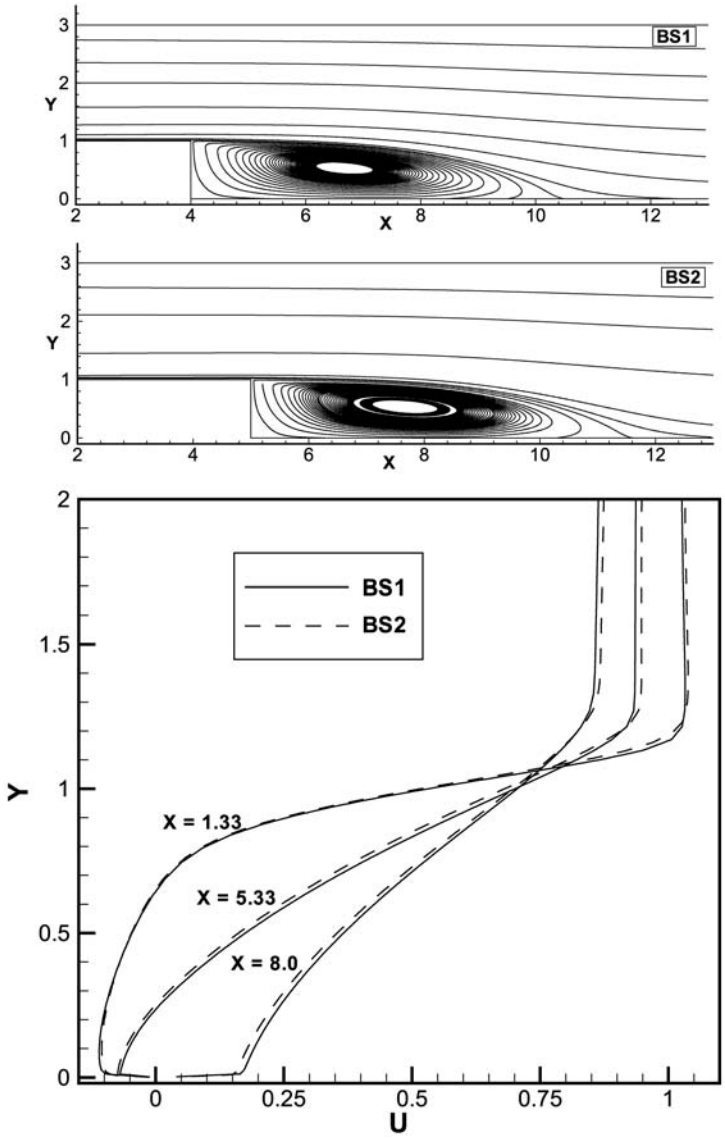

Figure 9.
A comparative study of the streamlines and the mean velocity profiles using BS1 and BS2 cases

The above two parameters are defined as the percentage in decreasing the current mixing length relative to R. In B and C cases, $L_S = L_T$. These two parameters are defined as:

$$E_S\% = \frac{R - L_S}{L_S} \times 100 \quad E_T\% = \frac{R - L_T}{L_T} \times 100 \tag{14}$$

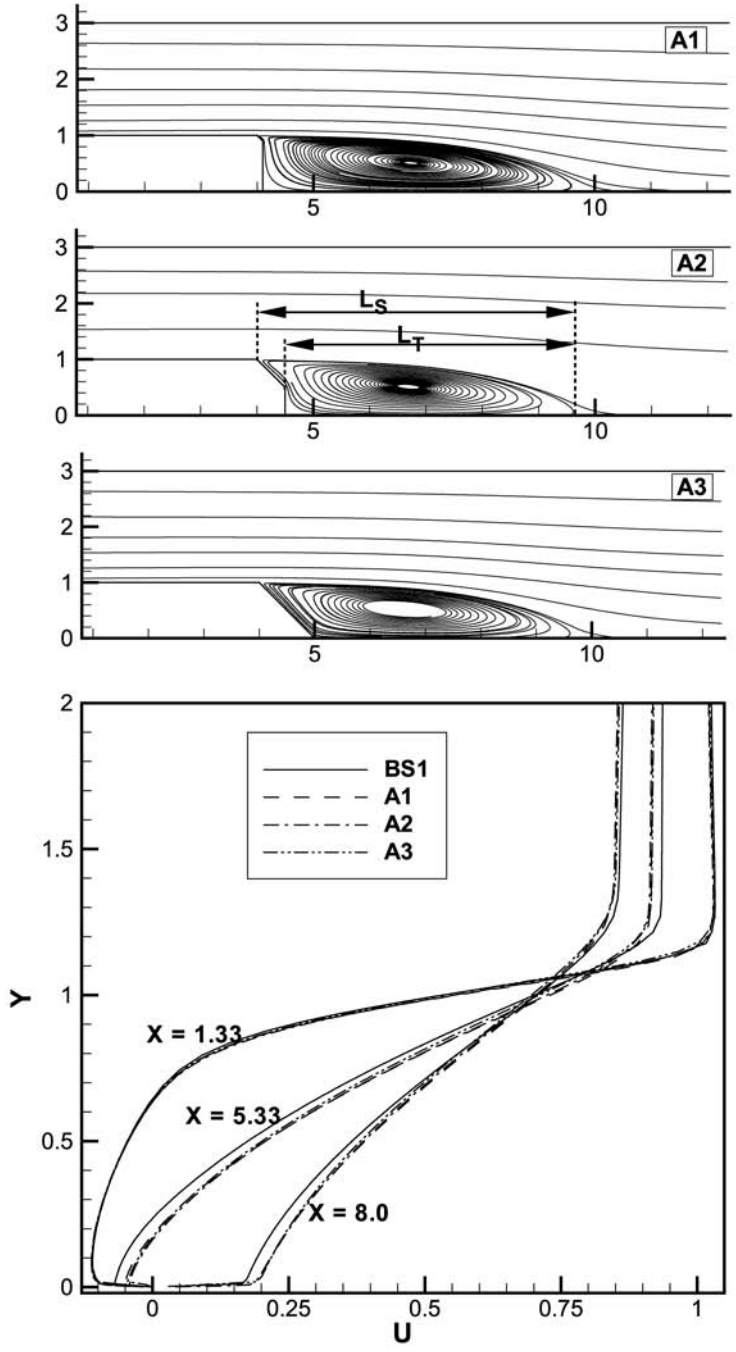

Figure 10.
A comparative study of the streamlines and the mean velocity profiles using A1-A3 cases

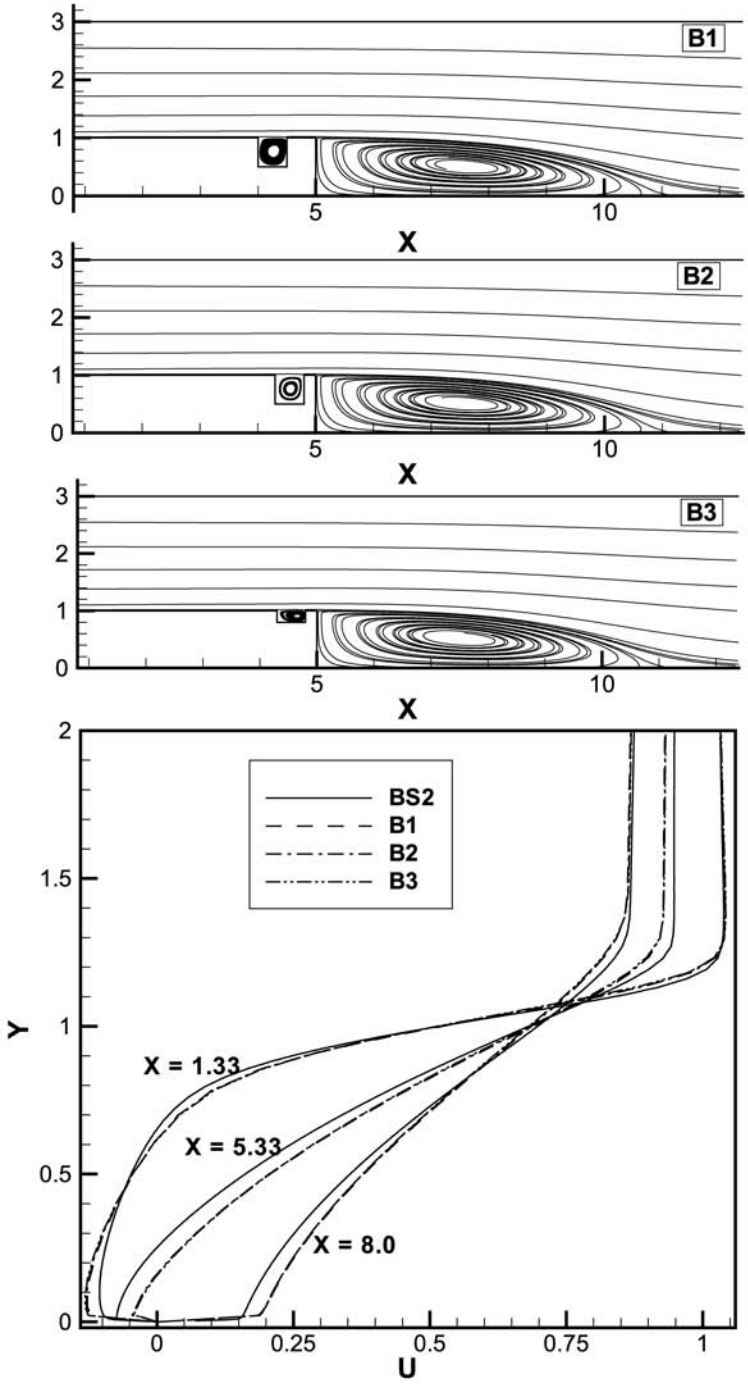

Figure 11.
A comparative study of the streamlines and the mean velocity profiles using B1-B3 cases

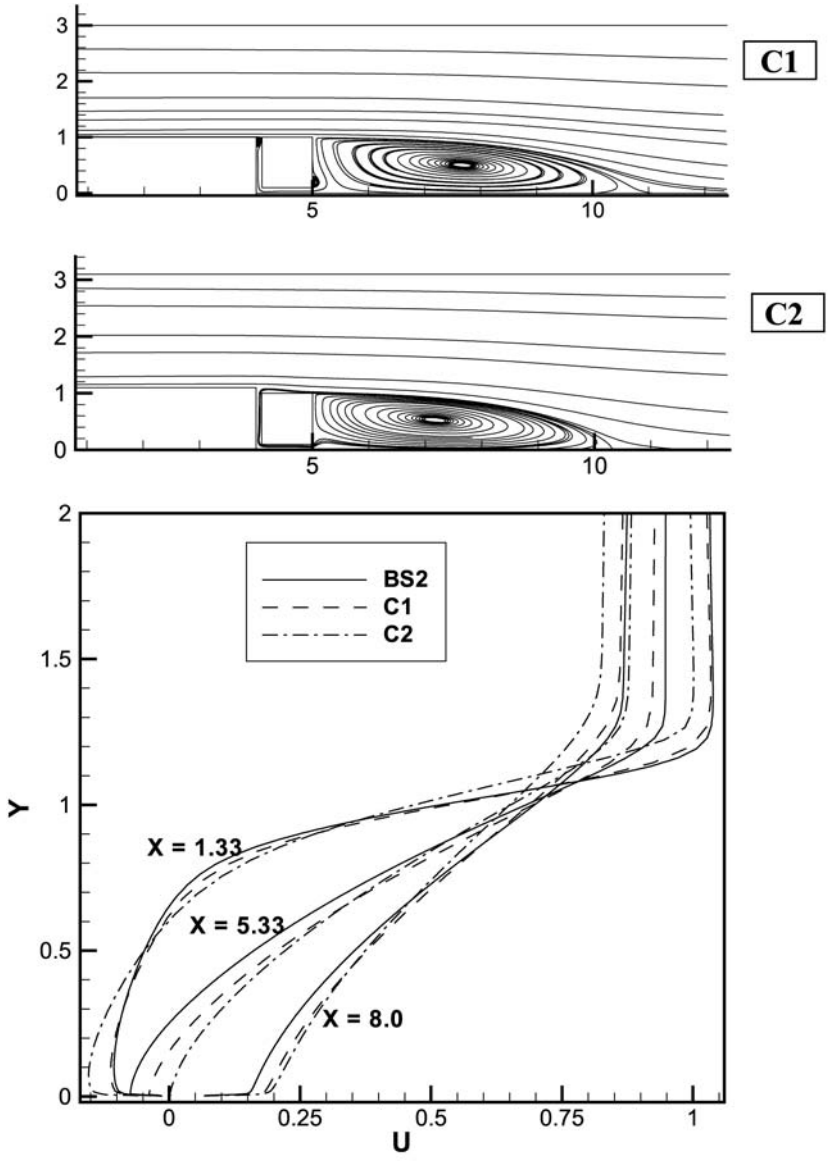

Figure 12.
A comparative study of the streamlines and the mean velocity profiles using C1 and C2 cases

Table III presents the amount of decrease in the length of separation region using A, B, C, and D configurations. As is seen, the C2 geometry has the most reduction effect in L_S magnitude. The amount of the reduction is about 15 percent. The other configurations do not affect the reattachment point considerably. Similarly, the geometries A3 and D2 have had the most important impact in reducing the magnitude of L_T. Cases A2 and C2 are next to A3 and D2 in destabilizing the reattachment point.

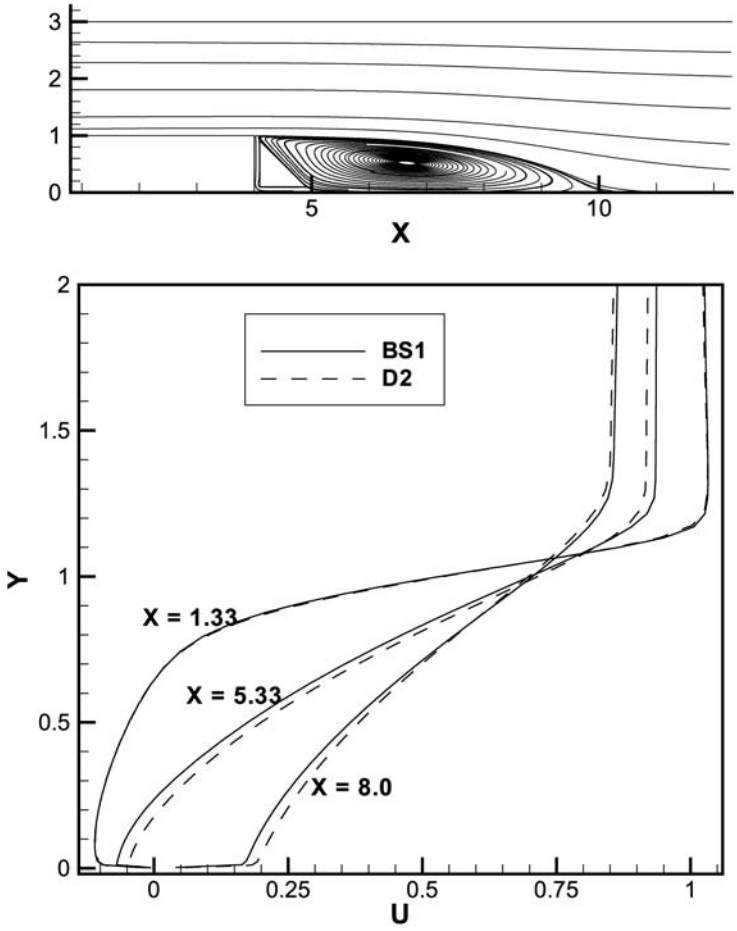

Figure 13.
A comparative study of the streamlines and the mean velocity profiles using D2 case

Type		L_S/h	E_T (percent)	L_T/h	E_T (percent)
A	1	5.7	7	5.6	9
	2	5.7	7	5.2	17
	3	5.7	7	4.7	30
B	1	5.7	7	5.7	7
	2	5.7	7	5.7	7
	3	5.7	7	5.7	7
C	1	5.7	7	5.7	7
	2	5.3	15	5.3	15
D	2	5.7	7	4.7	30

Table III.
The percentage of mixing length reduction using A, B, C, and D modified configurations

At the end, it is worth to mention that the current study is limited to 2D BFS geometries. However, the past experimental investigation on baseline BFS geometry has shown that the separated shear layer behind the step is firm and is not readily affected by the 3D influences if the BFS is wide enough in the spanwise direction. For example, Otugen (1991) performed a preliminary investigation before his measurements to insure 2D of the flow behind the step. He obtained the velocity and turbulence intensity profiles at different spanwise locations and showed that they were essentially the same regardless of the spanwise location. A similar study had been performed by Armaly *et al.* (1983). Nie and Armaly (2004) tried to reduce the width of BFS and study the impact of 3D of the flow on the main recirculation region behind the step. They performed measurements of the boundaries of the reverse flow regions that develop adjacent to the bounding walls of a 3D BFS flow as a function of Reynolds number. They say that the size of the reverse flow regions adjacent to the bounding walls is presented for the laminar, transitional, and turbulent flow regimes. In comparison with the reattachment point at the stepped wall for 2D flow, the 3D flow results at the center of the test section are slightly higher in the laminar flow regime ($Re < 400$), significantly lower in the transition flow regime ($400 < Re < 3,400$), and slightly lower in the fully turbulent flow regime ($Re > 3{,}400$). There is no spanwise variation in the turbulent regime and the distribution is almost uniform in the center width region for $0.2 < z/L < 1.8$. Additionally, the size of the reverse flow region adjacent to the sidewall and the flat wall in this geometry increases and moves further downstream in the laminar flow regime, decreases and moves upstream in the transition flow regime, and remains constant or diminishes in the turbulent flow regime; as the Reynolds number increases.

Conclusion

We employed a newly developed numerical algorithm capable of handling hybrid grid topologies to solve turbulent flow in irregular domains. Then, we used the extended tool to analyze the flow over modified BFS geometries in order to control the mixing regions and to evaluate the firm structure of the separated shear layer following the changes imposed in the baseline geometry of the step. Comparing the mean velocity profiles and the streamlines using quad and hybrid grid topologies indicated that they were nearly the same. The results obtained from different geometries indicate that the reattachment point is highly firm and is not easily affected by simple geometry modifications and simple trimming of the baseline configuration. However, a significant change in the baseline geometry, e.g. constructing suitable channels between the upstream and downstream of the step, may considerably affect the firm structure of the recirculating region.

References

Abbott, D.E. and Kline, S.J. (1961), "Theoretical and experimental investigation of flow over single and double backward facing steps", Report No. MD-5, Department of Mechanical Engineering, Stanford University.

Abu-Mulaweh, H.I., Chen, T.S. and Armaly, B.F. (2002), "Turbulent mixed convection flow over a backward-facing step – the effect of the step heights", *International Journal of Heat and Fluid Flow*, Vol. 23, pp. 758-65.

Amano, R.S. (1984), "Development of a turbulent near-wall model and its application to separated and reattached flows", *Numerical Heat Transfer*, Vol. 7, pp. 59-75.

Armaly, B.F., Durst, F., Pereira, J.C.F. and Schonung, B. (1983), "Experimental and theoretical investigation of backward-facing step flow", *Journal of Fluid Mechanics*, Vol. 127, pp. 473-96.

Baliga, B.R. and Patankar, S.V. (1983), "A control volume finite-element method for two-dimensional fluid flow and heat transfer", *Numerical Heat Transfer*, Vol. 6, pp. 245-61.

Bradshaw, F. and Wong, F.W.F. (1972), "Reattachment and relaxation of turbulent shear layer", *Journal of Fluid Mechanics*, Vol. 52 No. 1, pp. 113-5.

Darbandi, M. and Bostandoost, S.M. (2005), "A new formulation toward unifying the velocity role in collocated variable arrangement", *Numerical Heat Transfer; Fundamentals B*, Vol. 47 No. 4, pp. 361-82.

Darbandi, M. and Naderi, A.R. (2006), "Multiblock hybrid grid finite volume method to solve flow in irregular geometries", *Computer Methods in Applied Mechanics and Engineering*(in press).

Darbandi, M. and Schneider, G.E. (1998), "Analogy-based method for solving compressible and incompressible flows", *Journal of Thermophysics and Heat Transfer*, Vol. 12 No. 2, pp. 239-47.

Darbandi, M., Banaeizadeh, A. and Schneider, G.E. (2004), "Parallel computation of a mixed convection problem using fully-coupled and segregated algorithms", *American Society of Mechanical Engineers, Heat Transfer Division; HTD*, Vol. 375 No. 1, pp. 313-22.

Darbandi, M., Banaeizadeh, A. and Schneider, G.E. (2005), "Implicit finite-volume method to simulate reacting flow", AIAA Paper 2005-0574, the 43rd AIAA Aerospace Sciences Meeting and Exhibit, Reno, NV, January 10-13.

Darbandi, M., Schneider, G.E. and Naderi, A.R. (2003a), "The mesh orientation impact in performance of physical-based upwinding in structured triangular grids", *Proceedings of the 11th Annual Conference of the CFD Society of Canada (Vancouver, BC, Canada), CFDSC, Ottawa, ON, Canada*, pp. 688-95.

Darbandi, M., Schneider, G.E. and Naderi, A.R. (2003b), "A finite element volume method to simulate flow on mixed element shapes", AIAA Paper, 2003-3638.

Davidson, L. (1996), "A pressure correction method for unstructured meshes with arbitrary control volumes", *International Journal for Numerical Methods in Fluids*, Vol. 22, pp. 265-81.

Eaton, J.K. and Johnston, J.P. (1980), "Turbulent flow reattachment: an experimental study of the flow and structure behind a backward-facing step", Report No. MD-99, Thermoscience Division, Dep. Mech. Eng., Stanford University, Stanford, CA.

Eaton, J.K. and Johnston, J.P. (1981), "A review of research on subsonic turbulent flow reattachment", *AIAA Journal*, Vol. 19 No. 9, pp. 1093-100.

Heenan, A.F. and Morrison, J.F. (1998), "Passive control of back step flow", *Experimental Thermal and Fluid Science*, Vol. 16, pp. 122-32.

Ilinca, F. and Pelletier, D. (1999), "Positivity preservation and adaptive solution of two-equation models of turbulence", *International Journal of Thermal Sciences*, Vol. 38, pp. 560-71.

Kim, B.N. and Chung, M.K. (1994), "Experimental study of roughness effects on the separated flow over a backward-facing step", *AIAA Journal*, Vol. 33 No. 1, pp. 159-61.

Kim, D. and Choi, H. (2000), "A second-order time-accurate finite volume method for unsteady incompressible flow on hybrid unstructured grids", *Journal of Computational Physics*, Vol. 162, pp. 411-28.

Kim, J., Kline, S.J. and Johnston, J.P. (1984), "Investigation of reattaching turbulent shear layer: flow over a backward-facing step", *Journal of Fluid Engineering, ASME Transactions*, Vol. 102, pp. 711-24.

Kuhen, D.M. (1980), "Effects of adverse pressure gradient on the incompressible reattaching flow over a rearward-facing step", *AIAA Journal*, Vol. 18 No. 3, pp. 343-4.

Lien, F.S. and Leschziner, M.A. (1994), "Assessment of turbulence models including non-linear RNG eddy-viscosity formulation and second-moment closure for flow over a backward-facing step", *Computers & Fluids*, Vol. 23 No. 8, pp. 983-1004.

Nie, J.H. and Armaly, B.F. (2004), "Reverse flow regions in three-dimensional backward-facing step flow", *International Journal of Heat and Mass Transfer*, Vol. 47, pp. 4713-20.

Otugen, M.V. (1991), "Expansion ratio effects on the separated shear layer and reattachment downstream of a backward-facing step", *Experiments in Fluids*, Vol. 10, pp. 273-80.

Selby, G.V., Lin, J.C. and Howard, F.G. (1990), "Turbulent flow separation control over a backward-facing ramp via transverse and swept grooves", *ASME Journal of Fluid Engineering*, Vol. 112, pp. 238-40.

Sohn, J.L. (1988), "Evaluation of FIDAP on some classical laminar and turbulent benchmarks", *International Journal of Numerical Methods in Fluids*, Vol. 8, pp. 1469-90.

Thakur, S., Wright, J., Shyy, W., Liu, J., Ouyang, H. and Vu, T. (1996), "Development of pressure-based composite multigrid methods for complex fluid flows", *Progress in Aerospace Sciences*, Vol. 32, pp. 313-75.

Thangam, S. and Speziale, C.G. (1992), "Turbulence flow past a backward-facing step: a critical evaluation of two-equation models", *AIAA Journal*, Vol. 30, pp. 1314-20.

Westphal, R.V., Johnston, J.P. and Eaton, J.K. (1984), "Experimental study of flow reattachment in a single-sided sudden expansion", NASA TR 3765, Report MD-41, Stanford University, Stanford, CA.

Yang, Y.T. and Kuo, C.L. (1997), "Numerical study of a backward-facing step with uniform normal mass bleed", *International Journal of Heat and Mass Transfer*, Vol. 40 No. 7, pp. 1677-86.

Corresponding author
Masoud Darbandi can be contacted at: darbandi@sharif.edu